Nuclear Instruments and Methods in Physics Research B 383 (2016) 234–244

Contents lists available at ScienceDirect

Nuclear Instruments and Methods in Physics Research B

journal homepage: www.elsevier.com/locate/nimb

Imaging the attenuation coefficients of magnetically constrained positron beams in matter

Charles C. Watson

Siemens Medical Solutions USA, Inc., 810 Innovation Drive, Knoxville, TN 37932, USA

ARTICLE INFO

Article history:
Received 4 March 2016
Received in revised form 6 July 2016
Accepted 8 July 2016
Available online 7 August 2016

Keywords:
Magnetic field
Positron
Beam
Attenuation
Tomography
Imaging

ABSTRACT

This paper describes a method for tomographically imaging the linear attenuation coefficients (LACs) of positron beams in heterogeneous materials. A β^+ ray emitter such as ^{68}Ga, placed in a uniform 3T static magnetic field, generates a well-defined positron beam that maintains its spatial coherence over an attenuation of more than 10^{-3} while signaling its intensity via the annihilation radiation it generates. A positron emission tomography (PET) system embedded in the magnetic field measures the positron–electron annihilation distribution within objects illuminated by the beam. It's shown that this image can be decomposed into maps of the positron beam's flux and its material-dependent LACs without need for auxiliary measurements or transmission of the beam completely through the object. The initial implementation employs a hybrid PET/magnetic resonance imaging (MRI) scanner developed for medical applications. Mass thicknesses up to 0.55 g/cm^2 at a spatial resolution of a few millimeters have been imaged.

1. Introduction

The attenuation of β^+ rays in matter is a complex process that may involve inelastic electron scattering, elastic nuclear scattering, the formation of positronium, and ultimately, positron–electron annihilation. Measurements related to these interactions can provide useful information on material properties, such as the characterization of defect distributions in solids by means of positron lifetime spectroscopy [1]. Estimates of positron transport characteristics such as their ranges, LACs and stopping powers in known materials are important for practical applications such as PET [2,3], radiation shielding, and dosimetry [4]. The β-ray attenuation properties of a material are conventionally measured by placing uniform samples of varying thickness between a collimated β emission source and detector, and recording the transmission rate versus thickness [5,6]. One could envision extending this direct transmission method to three-dimensional (3D) β-ray transmission tomography, analogous to X-ray CT, but for β^+ rays, an alternative approach is feasible. This paper describes a novel 3D tomographic technique for non-destructively imaging β^+ ray attenuation coefficients in heterogeneous materials, referred to as *positron attenuation tomography* (PAT). It works by magnetically constraining positron beam divergence, and by using a PET camera to detect positron annihilations within the object being imaged rather than their transmission through it. The initial implementation employs a hybrid PET/MRI scanner developed for medical imaging.

An integrated PET/MRI consists of a PET system embedded in the uniform 3T $\mathbf{B}_0$ magnetic field region of an MRI scanner, as indicated schematically in Fig. 1a. When a ~1 MeV β^+ decay source such as ^{68}Ga ($E_{max} = 1.9$ MeV) is exposed within the field of this magnet, the emitted positrons follow helical paths around the field lines with gyroradii on the order of 1 mm or less due to the action of the Lorentz force, and a non-diverging positron beam is formed parallel to $\mathbf{B}_0$ across the PET's field of view (FOV) [7]. Losses in air are modest (~1%/cm) and thus a vacuum system is not required for beam transport. The PET component can accurately image the annihilation rate along the beam within an object intersecting it by detecting the annihilation radiation generated. Such a material structure is shown in Fig. 1b. The PET image of the annihilations produced by the beam in this object is shown in Fig. 1c. The annihilation rate per unit volume quantified in a voxel of this image, λ, can be understood as the product of the axial positron flux, ϕ_z, and the LAC of the material at that point, μ_z. Further, since the only

Abbreviations: PET, positron emission tomography; PAT, positron attenuation tomography; MRI, magnetic resonance imaging; CT, computed tomography; LAC, linear attenuation coefficient; FOV, field of view; PS, polystyrene; PE, polyethylene; FWHM, full width at half maximum; BSC, beam softening correction; 3D, three-dimensional.

E-mail address: charles.c.watson@siemens.com

http://dx.doi.org/10.1016/j.nimb.2016.07.008
0168-583X/

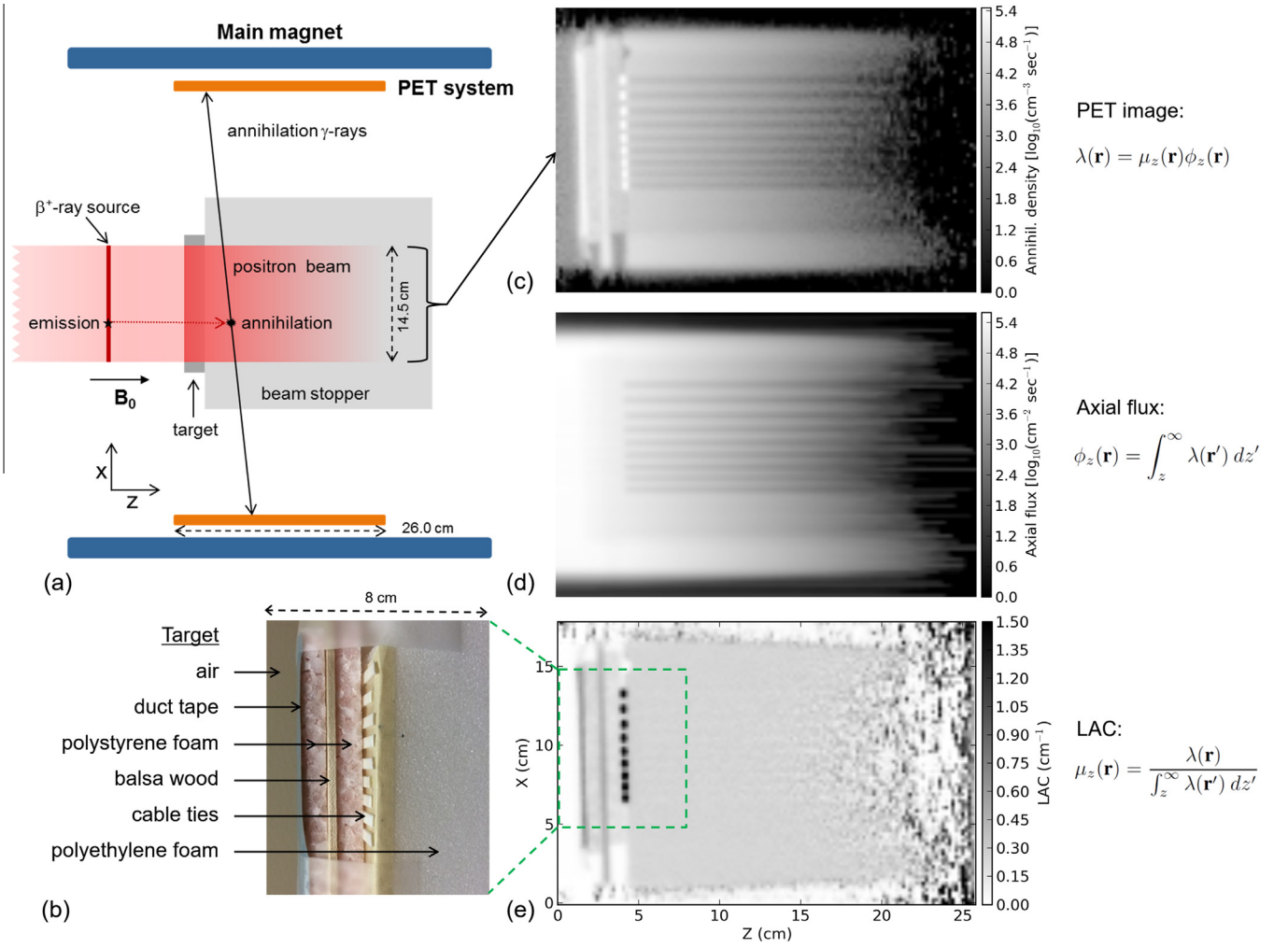

Fig. 1. (a) Schematic of an axial cross-section through the experimental configuration for positron attenuation tomography in a PET/MRI scanner (not to scale). (b) A material structure to be imaged. (c) The PET image of the annihilation rate density in the target and beam stopper. (d) The estimated positron axial flux. (e) The PAT image of the LAC distribution in the structure. The equations describe the relation between these images.

loss mechanism of positrons from the beam is annihilation with an electron, if the beam is fully stopped within the PET's FOV, the positron flux at any point can be estimated from the integral annihilation rate down-beam from that point, as shown in Fig. 1d. These two facts allow the flux and LAC components of the annihilation rate image to be distinguished. The resulting PAT LAC image is shown in Fig. 1e.

This paper begins with a discussion of the theoretical basis of PAT. Its implementation on a commercial PET/MRI system is then described, and LAC images of some example material structures are shown. The spatial coherence of the beam and the variation of the LACs due to beam softening are characterized. The issues of positron backscattering and the dependence of the image on view angle are illustrated. Supporting Monte Carlo simulations are also presented. Finally, some potential extensions and applications of PAT are discussed.

2. Theory

The attenuation of magnetically constrained positrons in matter can be discussed in terms of their axial flux $\phi_z(\mathbf{r})$ and a corresponding linear attenuation coefficient $\mu_z(\mathbf{r})$. In Appendix A it is shown that subject to certain approximations, the velocity integrated transport equation for the positron phase space density can be reduced to:

$$\frac{\partial \phi_z(\mathbf{r})}{\partial z} = -\mu_z(\mathbf{r})\phi_z(\mathbf{r}) \tag{1}$$

with

$$\mu_z(\mathbf{r}) = \frac{\phi(\mathbf{r})}{\phi_z(\mathbf{r})}\left(\frac{\rho_e(\mathbf{r})}{\phi(\mathbf{r})}\int \sigma_{\mathrm{an}}(\mathbf{r}, v)\, v f(\mathbf{r}, \mathbf{v})\, d\mathbf{v}\right). \tag{2}$$

Here $\mathbf{r} = (x, y, z)$ and $\mathbf{v} = (v_x, v_y, v_z)$ are spatial position and velocity vectors respectively, $f(\mathbf{r}, \mathbf{v})$ represents the number of positrons per unit phase space volume at $(\mathbf{r}, \mathbf{v})$, $v = \|\mathbf{v}\|$, $\rho_e(\mathbf{r})$ is the electron density, and the annihilation cross-section σ_{an} is a material property representing an average over electron states present. $\phi_z(\mathbf{r}) = \int v_z f(\mathbf{r}, \mathbf{v}) d\mathbf{v}$ is the net velocity-integrated positron flux in the axial (z) direction, and $\phi(\mathbf{r}) = \int v f(\mathbf{r}, \mathbf{v}) d\mathbf{v}$ is the total velocity-integrated flux. The factor in brackets on the right in (2) is the total flux-weighted average macroscopic annihilation cross-section of the material for the beam, Σ_{an}. In conventional narrow-beam transport scenarios the axial flux is attenuated both by scattering of particles out of the beam and their absorption within it. Here, due to the magnetic confinement, only absorption (annihilation) contributes to beam loss, but this loss is incurred by the total flux rather than just its axial component, resulting in the flux-ratio pre-factor in (2). As a consequence of this magnetic constraint, the material LACs accessible to PAT could differ from those measured by other techniques.

Because positrons can only leave the beam through annihilations detected by the PET camera, the annihilation rate density estimated in a PET image, $\lambda(\mathbf{r})$, must be related to $\mu_z(\mathbf{r})$ and $\phi_z(\mathbf{r})$ by

$$\lambda(\mathbf{r}) = -\frac{\partial \phi_z(\mathbf{r})}{\partial z} = \mu_z(\mathbf{r})\phi_z(\mathbf{r}) \tag{3}$$

Assume the beam propagates in the positive z direction and is fully absorbed by the point $z_0(x,y)$ within the PET FOV. Integrating (1) from z to z_0 and substituting $\lambda = \mu_z\phi_z$ from (3) yields

$$\phi_z(\mathbf{r}) = \int_z^{z_0} \lambda(\mathbf{r}')\, dz' \tag{4}$$

$$\mu_z(\mathbf{r}) = \lambda(\mathbf{r})\left[\int_z^{z_0} \lambda(\mathbf{r}')\, dz'\right]^{-1}, \quad z < z_0(x,y) \tag{5}$$

and thus both $\phi_z(\mathbf{r})$ and $\mu_z(\mathbf{r})$ are determined from the measured image data $\lambda(\mathbf{r})$ everywhere these data are non-zero.

Because the measured data are actually spatially discrete, the estimates of μ_z and ϕ_z are generated from discrete approximations to these equations in practice. Each value in the PET image represents the average annihilation rate density within a 3D voxel. The net axial flux entering a voxel at axial position z_n on its up-beam side is estimated from a sum of the image values in and down-beam from the voxel: $\phi_z(z_n) = \sum_{k=n}^{N} \lambda(z_k)\,\Delta z$, where N is the number of axial voxels in the image, and Δz is the pitch of the voxel in z. The mean flux in the voxel is estimated as the average of the values on its two axial boundaries, which for z_n are $\phi_z(z_n)$ and $\phi_z(z_{n+1})$. The value of μ_z in the voxel is then estimated as the ratio of $\lambda(z_n)$ to this mean axial flux:

$$\widehat{\mu}_z(z_n) = 2\lambda(z_n)/[\phi_z(z_n) + \phi_z(z_{n+1})], \quad n < N. \tag{6}$$

Aside from the effect of discretization, variations in μ_z at scales less than the spatial resolution of the PET camera, ℓ, can not be accurately estimated from a single λ image. Further, the resolution sets a limit on the maximum value of μ_z in a uniform object that can be practically imaged. If α is the greatest attenuation of the beam at which a useful image can be acquired, then the LAC must not be so large as to cause an attenuation greater than α in a distance ℓ, i.e., we must have $\mu_z < \ln(1/\alpha)/\ell$.

$\mu_z(\mathbf{r})$ is a functional of $f(\mathbf{r},\mathbf{v})$ and thus may depend on beam as well as material characteristics. In fact, it is observed empirically that as the beam penetrates a uniform object, the measured $\mu_z(\mathbf{r})$ increases with depth. A characterization of this "beam softening" effect, and a description of the correction implemented for it, are given in Section 5.3.

3. Materials and methods

3.1. Implementation and example images

PAT has been implemented on a hybrid 3T PET/MRI medical scanner (Siemens Biograph mMR). The PET component has a 26 cm axial FOV centered within the 45 cm long uniform field region of the main magnet (Fig. 1a). Its nominal full width at half maximum (FWHM) spatial resolution for a point source near the center of the FOV is 4.2 mm. The beam sources were two 14.5 cm long, 3 mm diameter lines of bare hardened epoxy resin containing about 19 MBq of ^{68}Ge/^{68}Ga radioactivity each. They were placed approximately 15 cm outside the edge of the PET's axial FOV near its transverse center, and stacked vertically, giving a horizontal planar beam over 6 mm thick and 14.5 cm wide extending across the FOV. For certain experiments, as will be indicated, only a single line source was used. Uniform polymer foam blocks were used to absorb the beam after it passed through the object of interest. Although they are referred to as beam stoppers, they are also being imaged. Data acquisition times were 1000–1500 s per scan. The 511 keV annihilation photon data collected by the PET camera were reconstructed into an image array with a voxel size of 2.03 mm axially and 2.09 mm in the transverse plane, using a standard clinical 3D, ordered subset, estimation maximization, maximum likelihood algorithm with 3 iterations, 21 subsets and no post-smoothing. The small spatial anisotropy of the voxels is neglected for the image displays. No corrections for the attenuation or scatter of the annihilation radiation were needed. These effects were negligible for the materials employed because the LACs of 511 keV γ-rays are approximately 70 times smaller than those of the positron beams. It would of course be feasible to apply such PET corrections if the situation warranted it, e.g., for the near-surface imaging of denser materials. Unless otherwise noted, the LAC images have been corrected for beam softening as described in Section 5.3.

The first test structure is shown in Fig. 1b. This phantom consists of six material regions from left to right: duct tape, a polystyrene (PS) foam conglomerate (1 cm), balsa wood (3 mm), PS foam (1 cm), an array of nine plastic pieces, and a large uniform polyethylene (PE) foam block of density 0.0344 ± 0.0009 g/cm^3. The plastic pieces are sections of cable ties with their long axes normal to the plane of the image. Each piece is 1 mm thick and 5 mm wide. The eight spaces between the pieces were 5, 5, 4, 4, 3, 3, 2 and 2 mm in order from top to bottom.

LAC images of two additional example material structures were acquired. One was an array of plastic soda straws consisting of twenty-four straws with a diameter of 5.75 mm, and fifteen with a diameter of 7.67 mm. This array was mounted on the PE foam block described above, and a plastic bag filled with 3–5 mm diameter polystyrene foam beads placed above it. The third test object was the dried fiber skeleton of a *Luffa aegyptiaca* fruit, 75 mm in diameter, in front of a curved PE foam block. This skeleton is composed of a thick network of cellulose-like fibers in air with a mean pore size of perhaps one mm, and three larger air pockets.

3.2. Spatial coherence

As discussed in Appendix A, the theoretical justification of the PAT technique relies on the approximation that positron transport transverse to the magnetic field can be neglected. A quantitative assessment of the effect was made in an experiment in which the annihilation intensity image of a single 3 mm diameter horizontal line source beam in a uniform PE foam block was viewed edge-on. The vertical image planes intersecting the beam were summed, and the full width at half maximum of transverse beam profiles in this image were evaluated versus depth of penetration. A comparison was made to Monte Carlo simulations of a similar configuration.

3.3. Beam softening

For a ^{68}Ga generated beam in a polyethylene foam block, the measured LAC increases by more than a factor of 3 as the beam is attenuated by a factor of 10^{-3} (Fig. 3). This differs significantly from the reported quasi-exponential attenuation of unconstrained β-rays in matter measured using conventional differential transmission techniques [5,6,8,9]. Simulations described later suggest this is mainly due to a reduction in energy or "softening" of the velocity distribution of the β^+rays as they propagate. While this effect provides some potentially useful information on the beam (related to how much attenuation it has experienced), practical interpretation of $\mu_z(\mathbf{r})$ as a material property needs to account for this dependence, at least to first order, and thus a beam softening correction (BSC) is desirable.

To support the development of a BSC algorithm, a scan was performed of a phantom consisting of a uniform PE foam block (0.0344 g/cm^3) with one to four layers of Al foils placed in front. There was also a foil-free region. Each foil had a mass thickness of approximately 0.063 g/cm^2 which is equivalent to about 1.8 cm of the PE foam. A 1.3 cm thick PS foam block (0.021 g/cm^2), different from that used in the first experiment, was placed in front of the foils. The dual line positron beam penetrated the PS foam and the foils before being stopped in the PE foam block. The variation in attenuation through the regions with different LAC distributions provided the data needed to define a BSC algorithm.

3.4. Backscattering

If the velocity distribution of positrons in the beam depends on the composition of the material traversed, not just its total attenuation, the proposed BSC may lose accuracy. This could happen for example due to variation in the relative concentration of heavier nuclei, which have a higher probability of backscattering positrons. This effect could potentially change the energy distribution in the beam as well as the flux ratio factor in (2). An attempt was made to characterize such a backscatter effect by scanning a phantom containing two pairs of Cu and Al metal foils placed in different regions in front of the PE foam block. The estimated mass thicknesses of the individual foils were 0.063 g/cm^2 (Al) and 0.030 g/cm^2 (Cu). Between and in front of the foil layers were two blocks of the PS foam described above. The dual line source beam penetrated the PS foam and metal foils before being stopped in the PE foam. Profiles through the BSC LAC image of this phantom were compared to assess the dependence on the presence of the heavier metal nuclei.

3.5. View angle dependence

Even if lateral transport of the positrons can be neglected, the finite resolution of the PET camera, as well as the helical motion of the positrons in the beam, reduce the spatial accuracy of the observed data with respect to the basic relation $\lambda(\mathbf{r}) = \mu_z(\mathbf{r})\,\phi_z(\mathbf{r})$. This is particularly consequential in the transverse direction. As a result, the LAC image of an inhomogeneous object may depend on its orientation relative to the beam, especially if it contains finely spaced high-contrast parallel structures. This phenomenon was investigated by imaging four 24 mm cubes, each consisting of five 4.7 mm thick layers of polymer foam with paper backing between, placed in front of a uniform polymer foam block at orientations of 0°, 22°, −28° and 90° relative to the beam. If it were possible to make a forward model of the image formation process accurate enough to reproduce the effects observed, then the data from multiple view angles might be combined through an iterative reconstruction technique to correct artifacts and achieve improved spatial resolution. An initial attempt at such a model is described.

4. Simulations

A Monte Carlo positron transport simulation was undertaken to assess consistency between existing microscopic cross-section data and the macroscopic transport coefficient measured by PAT. It was performed using PENELOPE-2011 [10]. This code offers a detailed physics treatment of hard scattering events combined with a condensed simulation approach to soft interactions. It provides exact tracking of positron trajectories in a uniform magnetic field. The original PENCYL main program for simulations in cylindrical geometries was modified by the author to incorporate calls to the PENFIELD subroutine package for EM field tracking support. In addition, a track length flux tally was added, and the endpoints of the positron tracks were recorded as a surrogate for the positron annihilation density. The simulation was designed to efficiently capture the essential physics of the experiments described in this paper, but was not a detailed replica of any one of them.

A schematic of the simulation geometry is shown in Fig. 2a. A uniform 3T **B** field was parallel to the z axis. The simulated source was a circular annulus in air, transverse to z, centered at $z = 0$ cm, with mean radius of 10 cm, and axial and radial thicknesses both 0.3 cm. This is an adequate approximation to the experimental line source because this radius is approximately 100 time larger than the gyroradii of the positrons. The source material was modeled as polyvinyl acetate at 1.5 g/cm^3. Isotropic positron emissions were distributed uniformly throughout this ring. The region that extended from the source ring to $z = 15$ cm was air filled. The region from $z = 15$ to 100 cm consisted of PE foam with a density of 0.0344 g/cm^3. The region behind the source ring, from $z = -20$ to -0.15 cm, was filled with PE at 0.344 g/cm^3 to approximate the low-density materials on which the experimental source was mounted. The outer radius of the entire geometry was 20 cm.

The emission energy spectrum for the ^{68}Ga β^+ source was computed from the Fermi beta decay theory for allowed transitions, using the relativistic form of the Coulomb factor [8], and assuming maximum emission energies (intensities) of 0.8217 MeV (1.190%) and 1.8991 MeV (87.72%) [11]. It is shown in Fig. 8b.

Values of the simulation parameters EABS(1:3), C1, C2, WCC and WCR were 2.0e6, 2.0e6, 1.0e3, 0.05, 0.05, 1e3 and 1e3, respectively, for all regions. A value of ULDV = 1.0 for the upper limit on the amount of deflection over a step in the B field was deemed adequate after testing values as low as 0.02. 10^7 showers were simulated. Each positron was tracked until its kinetic energy fell below 1 keV, at which point an annihilation event was assumed to occur. Fig. 2b displays one of the positrons' tracks in terms of its transverse offsets from its mean position, and its energy, as it propagates along the z axis. This track was chosen for display because it had the greatest depth of penetration among the first 100 tracks simulated; it does not necessarily represent a typical

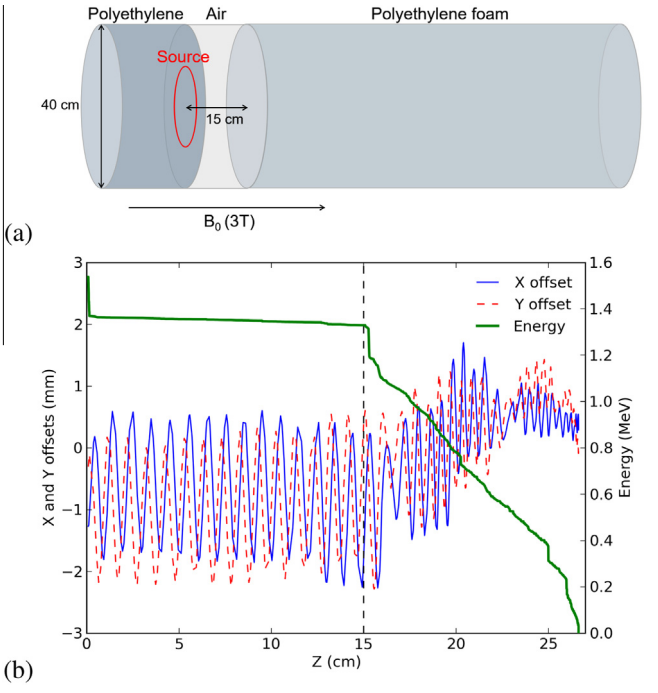

Fig. 2. (a) Schematic of the simulation geometry. (b) Positron position and energy along one track.

track. The vertical dashed line at 15 cm indicates the surface of the PE foam block.

This simulation was validated by comparing to the experiment performed with a single line source beam into a uniform foam block described in Section 3.2. Fig. 3a compares the simulated and measured positron annihilation density versus depth in the PE foam block. For this the measured intensity was averaged over the central part of the beam, and the simulated annihilation points were summed over transverse dimensions and histogrammed in 0.2 cm intervals along z. The z values in this figure refer to distance from the leading edge of the PET field of view. The surface of the foam block is at about 2 cm. The simulation results have been shifted in z and multiplicatively scaled to align them with the measured data. They have also been smoothed with a 4 mm FWHM Gaussian kernel to approximate the effect of the PET resolution. Fig. 3b shows the LACs estimated from the data corresponding to these intensity curves. As the beam enters the block, the simulated LAC values initially underestimate the measured ones by about 6% but show a somewhat more pronounced beam-softening effect with depth. This suggests some difference in the evolution of the energy spectra, which remains to be explored.

Fig. 4 compares the axial current (transversely integrated flux) estimated from the simulated annihilation density distribution as in (4), to that from a standard path length tally. Their agreement, as expected, serves to support the integrity of the Monte Carlo simulation as well as the validity of (4). Here z refers to the axial distance from the simulated source position. The surface of the foam block is at $z = 15$ cm. The annihilation density data here are the same as those shown in Fig. 3a, but unsmoothed.

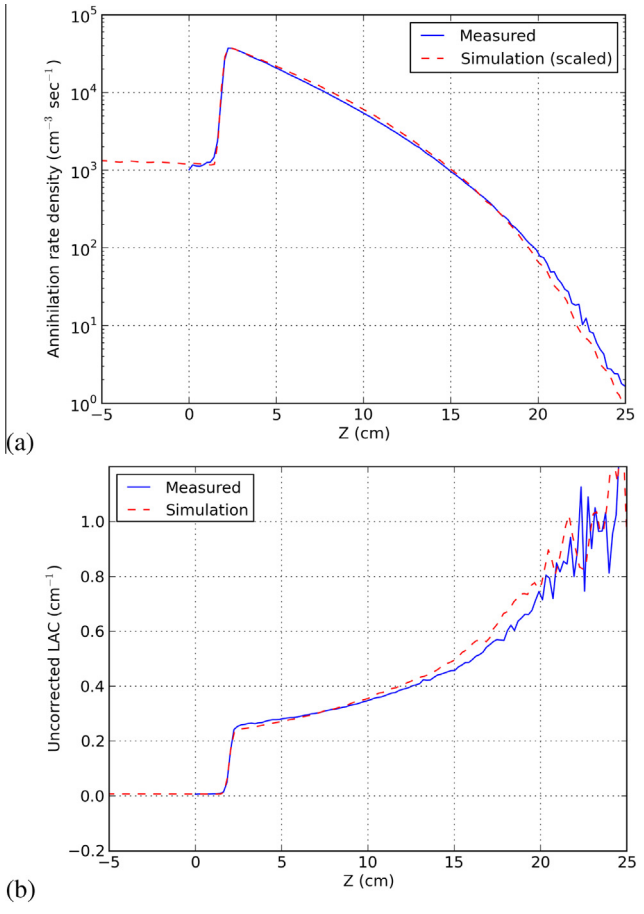

Fig. 3. (a) Comparison of measured and simulated positron beam intensity attenuation in a uniform PE foam block. (b) The LACs estimated from the annihilation intensities, uncorrected for beam softening.

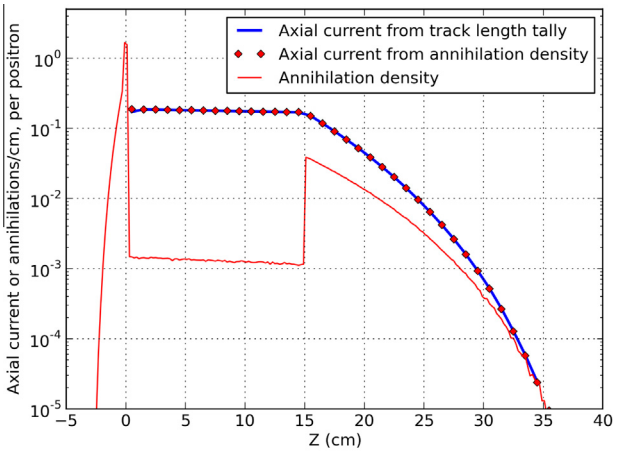

Fig. 4. Simulated positron current estimated from the annihilation density compared to a track length tally.

The radial widths of the simulated annihilation density distribution (beam) and the derived flux estimate were computed versus depth of penetration. For this the simulated annihilation points were histogrammed into radial and axial bins having widths of 0.1 and 4 cm respectively. The radial bins were normalized by their annular area, and the FWHM of the resulting radial profile computed for each axial interval. The positive, negative and net axial flux of positrons were estimated from the track length tally in the simulation, averaged over 1 cm intervals in z. The energy distributions of the positrons at two different penetration depths were computed: averaged over z intervals in the foam block at 15–18 and 27–30 cm from the source, and binned in 40 keV intervals in energy.

5. Results

5.1. Example material structures

Fig. 1c shows the logarithm of the positron annihilation rate density in the first test structure as imaged by the PET system. This is a two dimensional slice from a 3D image volume that has been averaged over three voxels (6.3 mm) normal to the plane. The beam enters from the left and produces annihilations in air before it enters the phantom. The shadows of the plastic pieces extend to their right, remaining distinct over the full range of the beam. In fact, the beam-to-shadow contrast increases with penetration depth due to the beam softening effect. This beam/shadow structure seems to confirm that MeV positron beams in a 3T field do largely maintain their transverse spatial coherence over nearly their full range, despite scattering.

Fig. 1d represents the axial positron flux within the object estimated from the integral transformation (4) of the data in Fig. 1c. Fig. 1e is the positron LAC image formed from the ratio of the data shown in Fig. 1c and d as in (5), and corrected for beam softening. The mean LAC value in the PE foam block is 0.240 ± 0.01 cm^{-1}, which is 5% higher than the value reported for the same material in [7], based on an exponential fit to the attenuation of a ^{68}Ga pill source beam. This μ value is equivalent to a mass attenuation coefficient $\mu/\rho = 6.98 \pm 0.29$ cm^2/g, where ρ is the mass density of the PE foam. The mass attenuation coefficient for ^{68}Ga β^+ particles in aluminum measured using a conventional differential transmission technique over the transmission range 0.20 to 0.01 has been reported to be 7.32 ± 0.22 cm^2/g [5]. For such techniques, only a

slight increase of μ/ρ with the atomic weight of the absorber is observed [8], suggesting that these measurements are in reasonable agreement.

The noisy region to the right in Fig. 1e occurs near the end of the beam's range, and is due to the statistical fluctuations in the annihilation rate density there observed by the PET camera. The apparent narrowing of the beam with depth is likely due to the tapering off of the beam's intensity at the ends of the line sources, causing it to fall more rapidly to the background noise level. The gaps between the plastic pieces are resolved down to 2 mm. The mottled textures of the PS foam pieces are consistent with their macro-cellular ($\sim$ 5 mm) structure. The apparent excess thicknesses of the duct tape and plastic pieces are a limitation of the PET resolution. Minimal residual beam-softening effect is observed. This and similar experiments in the bare uniform PE foam block (Figs. 3 and 6) show that a practical imaging depth of about 0.55 g/cm^2, equivalent to 16 cm of the PE foam, can be achieved with the sources used here. Dual-sided imaging could effectively double this accessible mass thickness.

The two additional LAC image examples are shown in Fig. 5. In the straw array of Fig. 5a the surface of the plastic bag and the straw walls are resolved, although the beads and 1–2 mm gaps between straws are not. The darker region of the plastic bag at the top (at arrow) is where it was folded over to form three plys. The cross-section of the *Luffa aegyptiaca* fruit in Fig. 5b shows mean LAC variations in this structure at a resolution of a few mm. These images have been corrected for beam softening and are displayed using bilinear interpolation between measured pixels.

5.2. Spatial coherence

The edge-on image of the 3 mm line source beam is shown in Fig. 6a, along with four exemplary profiles at the levels indicated in the image. Each row of this summed image was normalized to its maximum value, removing the primary effect of attenuation. The leading edge of the foam block is at 2 cm. The asymmetry of the profile broadening may be due to a small misalignment between the PET image space and the magnetic field lines. The full width at half maxima of transverse beam profiles in this image were evaluated over depth and are plotted in Fig. 6b versus the reciprocal attenuation factor as determined from a flux estimate. The FWHM increases approximately linearly, from 4.9 mm just inside the foam block to 6.3 mm at $z = 18$ cm, corresponding to a reciprocal attenuation factor of 250 and a 0.55 g/cm^2 total mass

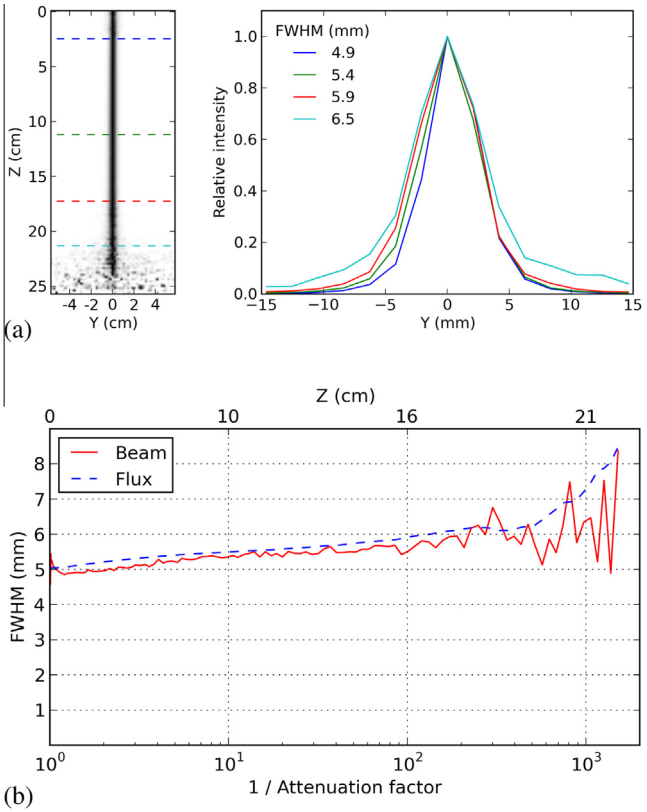

Fig. 6. (a) Normalized image of a positron beam in a PE foam block, and profiles through it. (b) Widths of the beam image and associated flux estimated as a function of attenuation.

thickness. The Monte Carlo simulations suggest that this coherence may be due to the fact that a typical positron slows down mainly through small angle deflections that permit it to approximately maintain its helical path. Occasional large angle scattering events may move the gyrocenter by some appreciable fraction of the gyrodiameter, but there are too few such events to permit significant transverse dispersion.

The divergence of a beam (i.e., its annihilation rate density image) across its range is not the most significant characteristic determining the accuracy of the PAT LAC estimate, however. The

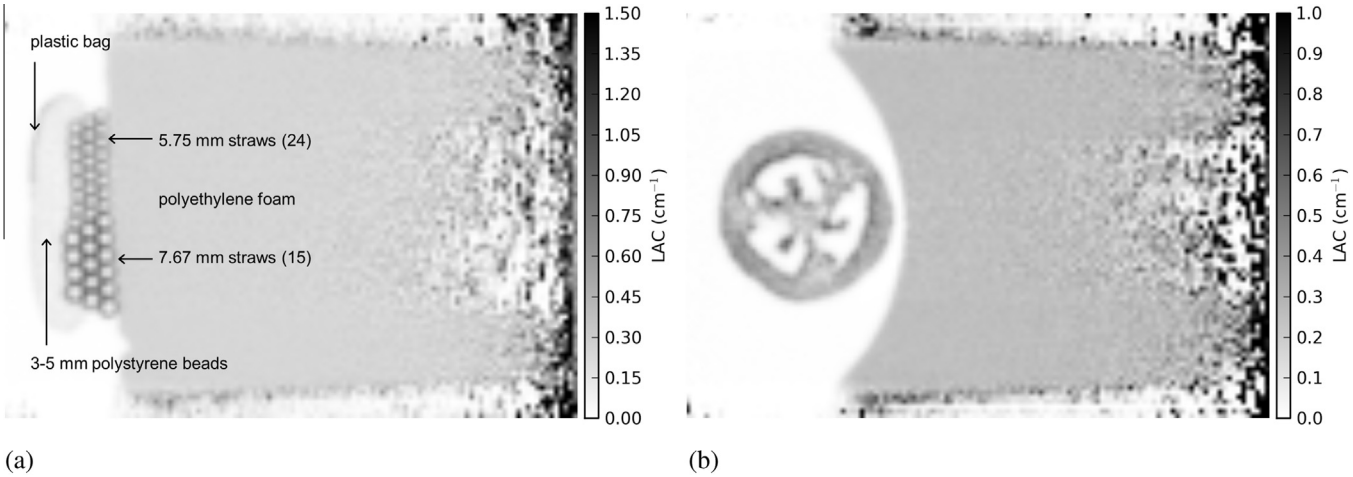

Fig. 5. (a) Positron LAC image of a straw array on a foam block. (b) LAC image cross-section of the fiber skeleton of a *Luffa aegyptiaca* fruit, 75 mm in diameter. The areas shown are 18 × 25 cm.

measured value of μ_z at a point z does not depend on the up-beam data, but only on whether the estimate of ϕ_z at that point, from the down-beam data, is consistent with $\lambda(z)$ in terms of their lateral averaging. To assess this, the FWHMs of the positron flux computed from the annihilation intensity data in Fig. 6a are also plotted in Fig. 6b. While both the λ and ϕ_z distributions increase in width by about 30% over an attenuation of 4×10^{-3} (at $z=18$ cm), the flux is only about 4% (0.2 mm) wider than the annihilation intensity on average. Similar trends are seen in the simulated data shown in Fig. 7, although the simulated beam and flux widths are about 1 mm smaller than the measured values, likely due to the spatial resolution of the PET camera. Here the vertical dashed line indicates the surface of the PE foam block. The LAC errors due to this difference between the spreading of the beam and estimated flux will depend on the annihilation intensity distribution but seem likely to be small except perhaps at sharp lateral discontinuities in μ_z.

5.3. Beam softening

The beam "softening" effect could arise from variation in either the angular or energy distribution of the positrons with depth of penetration. The positive, negative and net axial fluxes of positrons estimated from the track length tally in the simulation are shown in Fig. 8a as ratios to the total scalar flux. Outside the source (points plotted at 1.5 cm and greater), the negative (backward) flux of positrons decreases only slightly relative to the total flux over the beam's range, while the positive flux ratio increases from 0.4 to 0.55. The net flux ratio appears to approach a constant value of slightly less than 0.5 after traversing about 5 cm of foam. The surface of the PE foam block is at 15 cm. These results imply that the total-to-axial flux ratio pre-factor in (2) decreases by about 33% over the beam's range, and thus moderates rather than enhances the beam-softening effect.

The simulated energy spectra of the positrons at two different penetration depths are shown in Fig. 8b, together with the β^+ energy spectrum used as the source for the simulation. The mean mass depths of penetration (including the air between the source and foam) are indicated together with the mean energies of the spectra. The decreasing energy with penetration depth leads to increasing LAC because the annihilation cross section $\sigma_{an}(E)$ increases with decreasing E over the energy range of importance here [10]. Thus the simulations suggest that the primary reason for the increase of the positron LAC with attenuation, at least in uniform media, is a reduction in the energy of the flux rather than a change in its angular distribution.

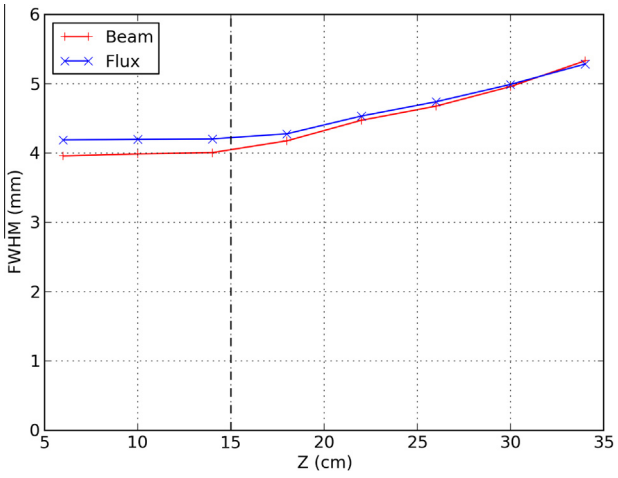

Fig. 7. Simulation results for beam and flux widths.

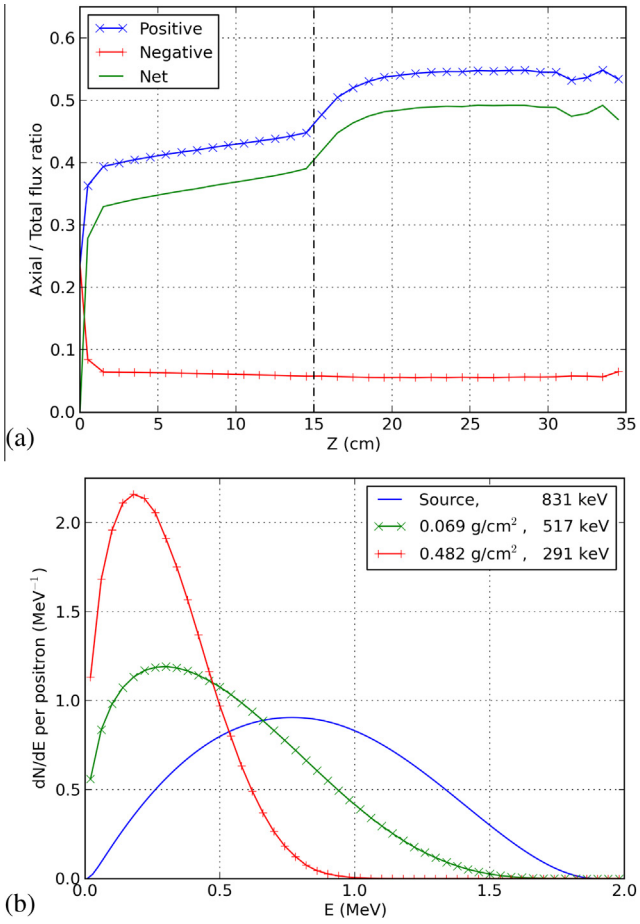

Fig. 8. Simulation results: (a) Axial flux ratios; (b) Energy spectra for the source, and the positron distribution at two depths; the mean energies and corresponding mass thicknesses are listed.

The BSC phantom study is shown in Fig. 9. The number of Al foil layers increases from 0 to 4 from top to bottom. The positron beam enters from the left. Fig. 9a is the raw LAC image generated from the PAT transform, i.e, with no correction for the beam softening effect. This slice is averaged over 2 pixels (4.2 mm) normal to the plane shown and represents an 18×26 cm region in the plane.

The LAC values reported in the PE foam vary substantially with depth, and with the number of Al foils penetrated. Axial (horizontal) profiles through this image are plotted as the solid lines in Fig. 9c. The line colors correspond to the position markers in Fig. 9a, and each profile represents a mean over 5 pixels (10.4 mm) vertically in the image, centered at its marker. Here the abscissa is $M_z(\mathbf{r})=\int_0^z \mu_z(\mathbf{r}')\,dz'$ rather than z, where $\mu_z(\mathbf{r}')$ is the uncorrected LAC. The motivation for this choice is that $\phi_z(\mathbf{r})=\phi_z(0)\exp[-M_z(\mathbf{r})]$, which follows from (1). Thus to the extent that the change in the observed LAC depends only on the total attenuation of the axial flux, it should be possible to characterize it in terms of $M_z(\mathbf{r})$, not unlike the beam-hardening correction made in X-ray CT. Indeed, the trends of increasing LAC in the uniform PE foam are very similar for all profiles. The black dashed curve in Fig. 9c is a least squares fit of a quadratic polynomial to a portion of the 'Foam' and 'Al×1' data in the uniform PE block, corresponding to $g[M_z(z)]=0.24+0.034\,M_z(z)+0.0037\,[M_z(z)]^2$. By removing this trend, raw LACs at any point may be corrected to the value they would have had, if they had been measured with the beam as it enters the PET FOV, by

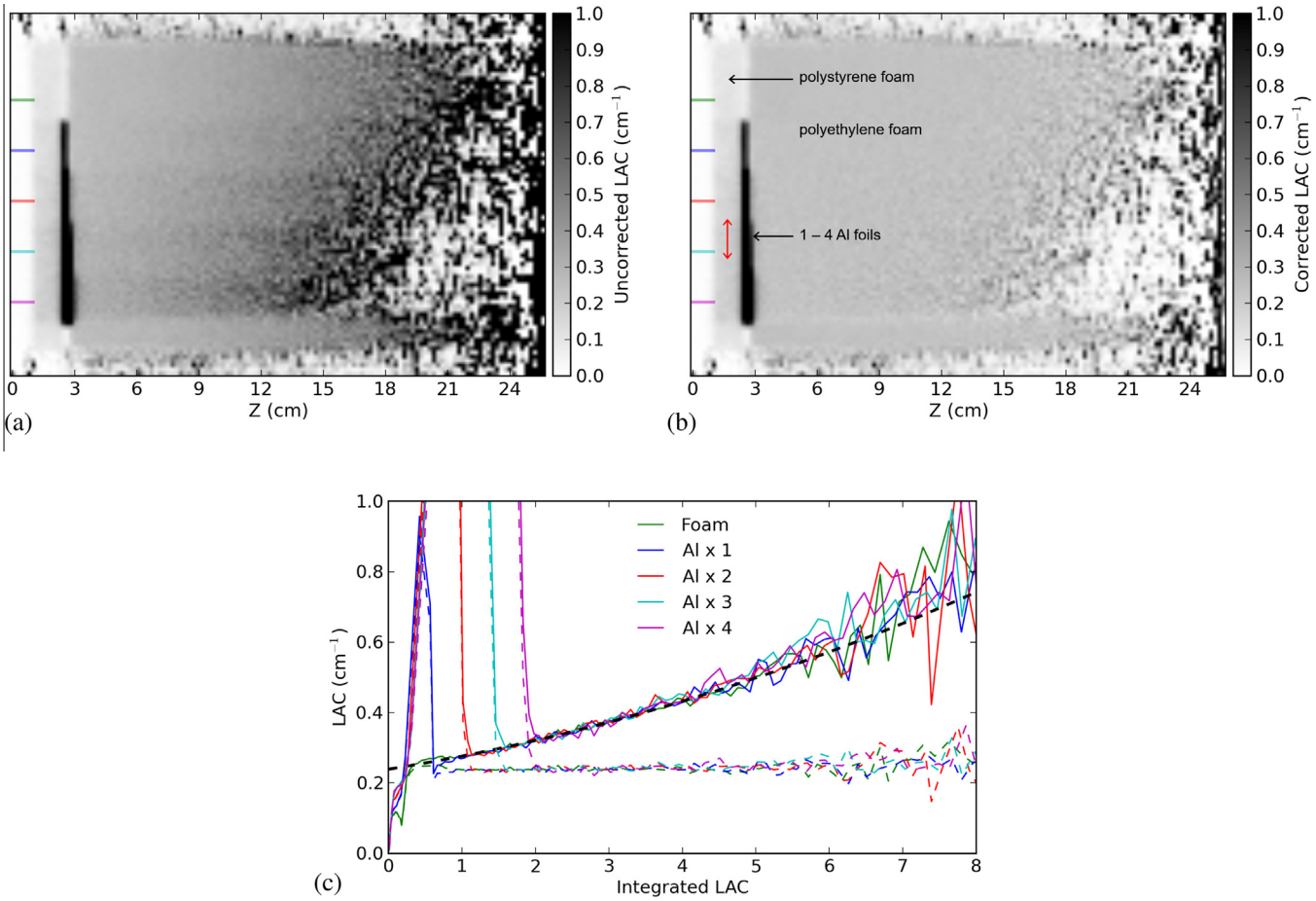

Fig. 9. Beam softening correction: (a) Uncorrected LAC image; (b) Corrected LAC image; (c) Profiles through the uncorrected (solid) and corrected (dashed) images at the levels indicated by the colored markers. (For interpretation of the references to colour in this figure legend, the reader is referred to the web version of this article.)

$$LAC_{\mathrm{BSC}}(z) = LAC_{\mathrm{raw}}(z)\left(\frac{g(0)}{g[M_z(z)]}\right). \tag{7}$$

The result of applying this LAC transform is shown in Fig. 9b, with corresponding profiles shown as the colored dashed curves in Fig. 9c. This same transform was used for all BSC results reported in this paper. However, because it only compensates for changes relative to the beam's state as it enters the FOV, it may depend on source characteristics, and thus could require recalibration for different measurement configurations.

5.4. Backscattering

Some evidence for enhanced backscattering can be seen in Fig. 9b to the left of the Al foils in the PS foam material (red double-sided arrow): the LAC appears to increase with the number of foils the beam encounters after passing through the foam. The dual foil backscattering study is shown in Fig. 10b. Here the Cu foil pair is on the bottom and Al foils in the center. No foils were present in the top third of the phantom. The image represents the BSC LAC in the phantom. Axial (horizontal) profiles through it are plotted in Fig. 10a. Each profile corresponds to the mean over a transverse region 0.83 cm thick (normal to the plane) and 2.71 cm wide, centered at the position of the marker of the same color in Fig. 10b.

The LAC values in the PS foam block in front of the first foil layer are substantially higher for the Cu and Al profiles than for the foam-only profile, and slightly higher for the Cu than for the Al foil profile (red arrows in Fig. 10). It seems clear that this effect must be due to changes in the positron velocity distribution as a result of enhanced backscattering from the foils relative to PS foam. Backscattering is due to elastic scattering from nucleii, and is more probable at lower energies [12], which would tend to lower the mean energy of positrons up-beam from the foil and thereby increase the average annihilation cross-section Σ_{an}. Further, the counter-flowing backscatter current would increase the total to axial flux ratio pre-factor in (2). Both these effects would cause μ_z to increase. The fact that the Cu foil produces a slightly larger effect than the Al foil despite having less than half its mass thickness is consistent with measured electron backscattering coefficients for these materials in this energy range [12].

The peak LACs reported in the foils are greatly reduced by resolution broadening, but the relative amplitudes for Cu and Al are consistent with their having similar mass attenuation coefficients. The difference in values between the front and rear foils may be a resolution or BSC inaccuracy effect. An interesting phenomenon is observed after the second foil layer at about 7 cm. Both the Cu and Al profiles underestimate the PE foam LAC, more so for the Cu than for the Al. However, the estimated LACs recover toward the correct value as the beam penetrates farther. A possible interpretation of this effect is that the beam has been hardened by passing through the metal foils due to the preferential removal of lower energy positrons by their enhanced backscattering. As it then propagates in the foam, down-scattering returns the energy spectrum to its 'normal' distribution for the amount of attenuation the beam has experienced.

In some applications, supplementary measurements may be desirable to detect and correct for such variability in beam characteristics. These might include the use of beams having different

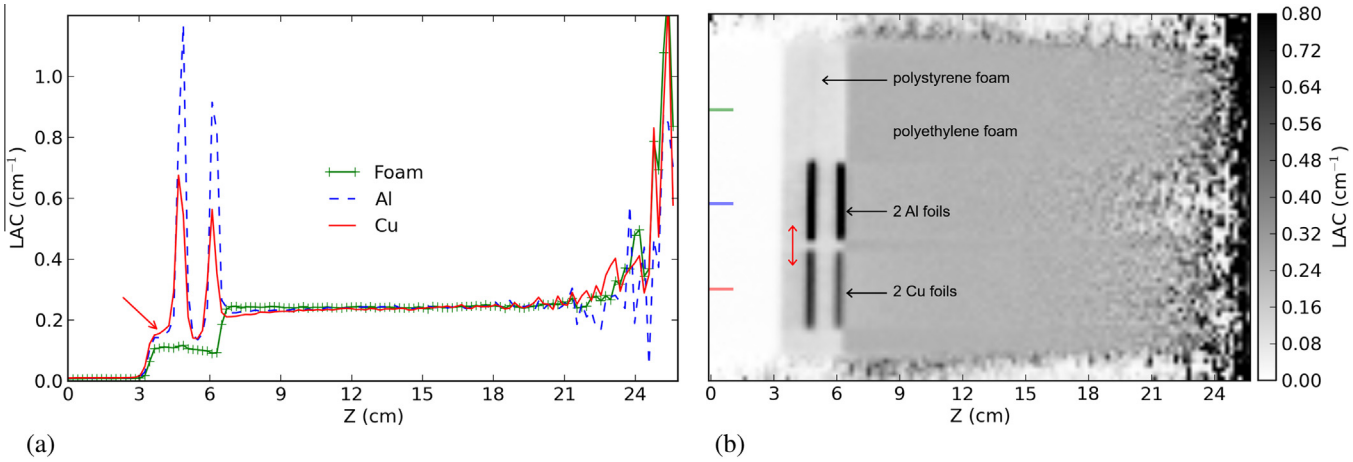

Fig. 10. (a) Horizontal profiles through the image on the right at the locations indicated. (b) LAC image for a positron beam passing through air, polystyrene foam, and Cu and Al foils before entering a polyethylene foam block.

energy spectra (from different radioisotopes, or variable filtering), or multi-angle imaging as discussed in Section 3.5.

5.5. View angle dependence

The positron LAC image of the four laminated foam cubes is shown as the 'Measured' data in Fig. 11. The beam enters vertically from the top. (All images in this section are displayed using nearest neighbor interpolation, so the actual pixel structure can be seen.) The loss of spatial resolution and LAC accuracy is most apparent when the layers are parallel to the beam.

To simulate these effects, an ideal LAC model of the laminated foam cube was initially generated in a two-dimensional (2D) array with 0.7 mm pixel dimensions. LAC values for the foam, 2-ply paper and air were 0.4, 5.0, and 0.008 cm^{-1}, respectively. The outer paper layers were single-ply. The LAC of the stopping block following the cube (not shown in the following images) was 0.23 cm^{-1}. To approximate the effect of the helical motion and scattering of the positrons, the ideal LAC distribution was blurred by filtering it with a symmetric 2D Gaussian kernel having a FWHM of 1.0 mm. The resulting LAC model is shown in Fig. 12a for the case with the laminae parallel to the beam direction. An annihilation intensity distribution was then estimated by multiplying the LAC image by its exponentiated negative cumulative integral along the beam, representing positron propagation without beam softening. To simulate PET imaging resolution, this annihilation rate distribution was smoothed with a 2D Gaussian kernel having FWHMs of 3.5 and 2.5 mm transverse and parallel to the beam, respectively. The resulting estimated annihilation rate density image is shown in Fig. 12b. The native pixel size for the reconstructed PET image data is about 2.1 mm, or three times larger than the pixels in Fig. 12b. To model this, the annihilation image was rebinned by a factor of 3 in both dimensions using pixel averaging. This resulted in the modeled PET image shown in Fig. 12c. From this image (including the stopping block) an estimated LAC distribution was computed from the PAT transform (5), and is shown in Fig. 12d. This is one of the estimates shown as the 'Modeled' data in Fig. 11; the others were generated in the same way following rotation of the ideal model to the appropriate angle. They show structure and contrast very similar to the measured images. The variation in appearance with orientation carries information on

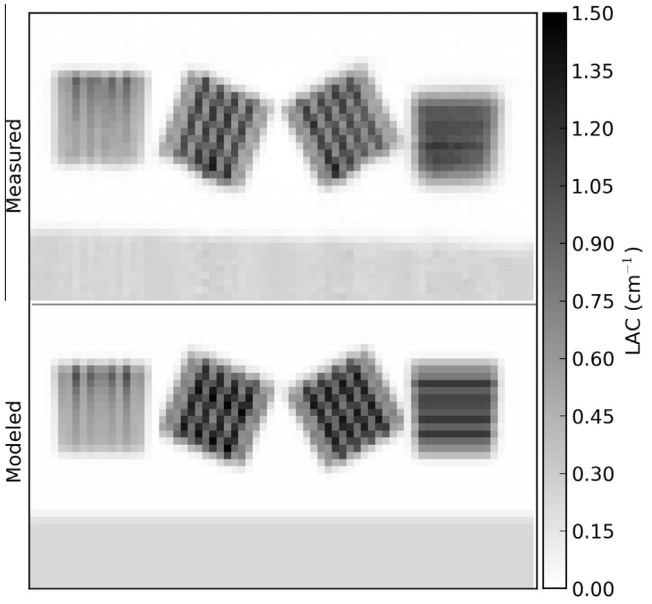

Fig. 11. Measured and modeled LAC images of 24 mm laminated foam cubes at angles of 0°, 22°, −28° and 90° relative to a vertical beam.

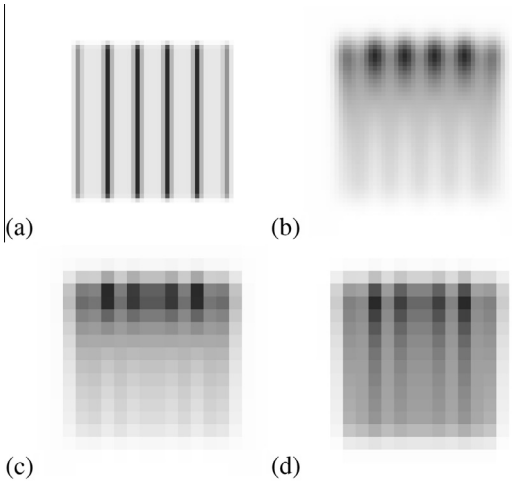

Fig. 12. (a) Model LAC after blurring. (b) Annihilation rate image post smoothing, and (c) rebinned to PET resolution. (d) LAC image estimated by applying the PAT transform.

structure beyond what can be determined from any single view. The ability to model the PAT imaging process suggests that it may be possible to exploit this information to improve the spatial resolution of the LAC images. This will be a direction for future research.

6. Discussion and conclusions

PAT is a step forward in the ability to image positron annihilation cross-sections in 3D not unlike the progress X-ray CT brought to the volumetric measurements of Compton and photoelectric cross-sections. The key physics leveraged by PAT is that a magnetic field of sufficient strength can maintain a β^+ ray beam's collimation as it penetrates matter, and that, as a consequence, detection of its annihilation rate density distribution also determines its axial flux. PAT thus offers the unique advantages that no separate measurement of incident flux is required, and that the near-surface regions of objects the beam does not fully penetrate can still be imaged. The experimental results presented are strongly supported by the simulations discussed, and there is good evidence that techniques for enhancing quantitative accuracy, such as corrections for beam softening and multi-angle imaging, are viable.

Positron beams with a wide range of sizes and cross-sectional shapes can be constructed [7]. Higher energy β^+ decay or accelerator sources could increase the depth of investigation, while lower energy ones could increase sensitivity. Higher strength sources could reduce acquisition times by an order of magnitude or more. Higher strength magnetic fields could likely improve the transverse resolution capability of the beams, although in the current implementation the limiting factor is the PET resolution. MR-compatible PET detection systems with higher spatial resolution capability than the one described here already exist, however. A BrainPET MR insert (Siemens) with 2.8 mm FWHM spatial resolution operating in a 9.4 T magnet has already been used for PET imaging of ^{120}I ($E_{max} = 4$ MeV) [13]. There are currently over 100 PET/MRI systems worldwide on which PAT could be readily performed.

In addition to imaging the structure of lightweight materials as demonstrated here, density variations in compressed elastic media have also been observed. The LAC of air can be measured with ^{68}Ga (e.g., Fig. 10), but ^{18}F β^+ ray beams ($E_{max} = 0.635$ MeV) have μ/ρ values over four times higher [7] and thus even greater sensitivity, making quantitative imaging of gas flow structure feasible. Gas and fluid flow through low-density porous media could also be visualized. In the context of beta emission imaging of plant and animal tissues, the beam softening effect may offer a means for correcting the confounding influence of beta attenuation. Because the transport properties of high energy electrons and positrons are similar [8,9], applications of PAT in radiation shielding and dosimetry for both electrons and positrons seem obvious. PAT may also contribute to the understanding of anisotropic positron range effects in PET/MRI studies [14]. Other areas that would be of interest to explore with PAT include the possible effects on positron transport of electric charge and microscopic structure [15] in materials. Additional applications in medical diagnostics, materials science, biological research and industry remain to be defined, but it's fair to say that PAT has already proven useful in illuminating the physics of magnetically constrained positron beam propagation in matter and can be a valuable tool for developing a better understanding of this phenomenon.

Acknowledgements

I would like to thank Nancy Watson and Christine Lorenz for their support and helpful suggestions.

Appendix A

A.1. Transport theory

Although solution of the Boltzmann equation for charged particle transport in neutral media with an imposed magnetic field is an area of active research in mathematical physics [16,17], this work primarily focuses on the diffusion of low energy (<100 eV) positron swarms, and does not explicitly relate annihilation rate densities to velocity-integrated transport coefficients, which is the physics underlying PAT. Therefore a derivation of this relation for the source-free steady-state problem is given here, based on the assumption that diffusion transverse to the field due to scattering can be neglected. The justification for this assumption is discussed in Section 5.2.

Consider a cylindrical PET system situated in a static, uniform magnetic field $\mathbf{B}$, with the PET scanner's axis parallel to its field lines along the z axis, as in Fig. 1a. A positron beam produced by an external β^+ decay source passes through the scanner, and maintains a macroscopic steady-state positron distribution in a stationary object placed within the FOV. Let $f(\mathbf{r},\mathbf{v})$ represent the number of positrons per unit phase space volume at $(\mathbf{r},\mathbf{v})$, where $\mathbf{r} = (x,y,z)$ and $\mathbf{v} = (v_x, v_y, v_z)$ are spatial position and velocity vectors respectively. The time-independent, homogeneous Boltzmann transport equation for f is:

$$\mathbf{v}\cdot\nabla_{\mathbf{r}} f(\mathbf{r},\mathbf{v}) + \frac{d\mathbf{v}}{dt}\cdot\nabla_{\mathbf{v}} f(\mathbf{r},\mathbf{v}) = D_c f \tag{8}$$

where t is time, ∇ is the gradient operator, and D_c is a collision operator. In a magnetic field, the second term is the rate of change in f due to acceleration of the positrons by the Lorentz force, $q(\mathbf{v}\times\mathbf{B})$, where q is the positron's charge. Expressing $\nabla_{\mathbf{v}}$ in cylindrical coordinates, and considering that the force is normal to both $\mathbf{v}$ and $\mathbf{B}$, this term becomes:

$$\frac{q}{m}(\mathbf{v}\times\mathbf{B})\cdot\nabla_{\mathbf{v}} f(\mathbf{r},\mathbf{v}) = \frac{qB}{m}\frac{\partial f(\mathbf{r},\mathbf{v})}{\partial\varphi_v} \tag{9}$$

where m is the positron's (relativistic) mass, and φ_v is the azimuthal angle of its velocity.

In the absence of deviations due to scattering, a positron follows a helical path around the $\mathbf{B}$ field lines. Its motion transverse to $\mathbf{B}$ is a circular orbit in the (x,y) plane at constant speed, with angular velocity $\omega = qB/m$. A total derivative of f along this transverse path may written in terms of φ_v:

$$\frac{df}{d\varphi_v} = \frac{\partial f}{\partial x}\frac{\partial x}{\partial\varphi_v} + \frac{\partial f}{\partial y}\frac{\partial y}{\partial\varphi_v} + \frac{\partial f}{\partial\varphi_v}. \tag{10}$$

Multiplying through by ω and recognizing that $\omega(\partial x/\partial\varphi_v) = v_x$, etc., gives

$$\omega\frac{df}{d\varphi_v} = v_x\frac{\partial f}{\partial x} + v_y\frac{\partial f}{\partial y} + \frac{qB}{m}\frac{\partial f}{\partial\varphi_v}. \tag{11}$$

The right hand side of (11) comprises the transverse gradient terms in (8). So, to the extent that transverse deviations due to scattering can be neglected, the transport equation can be written as:

$$\omega\frac{df}{d\varphi_v} + v_z\frac{\partial f}{\partial z} = D_c f. \tag{12}$$

Since the measurements available in the proposed methodology do not distinguish positron velocity, this equation may be integrated over velocity. Doing this, the first term vanishes. The second term becomes $\partial\phi_z(\mathbf{r})/\partial z$, where $\phi_z(\mathbf{r}) = \int v_z f(\mathbf{r},\mathbf{v})\,d\mathbf{v}$ is the net velocity-integrated positron flux in the axial (z) direction. The collision term on the right represents the rate of change of the

positron phase space density due to scattering and annihilation interactions. When integrated over velocity, only changes in spatial density remain, and this density can only decrease due to annihilations, leading to:

$$\int D_c f(\mathbf{r},\mathbf{v})\,d\mathbf{v} = -\rho_e(\mathbf{r}) \int \sigma_{\mathrm{an}}(\mathbf{r},v)\,v f(\mathbf{r},\mathbf{v})\,d\mathbf{v} \tag{13}$$

where $v = \|\mathbf{v}\|$, $\rho_e(\mathbf{r})$ is the electron density, and the annihilation cross-section σ_{an} is to be understood as a material property representing an average over electron states present.

The velocity-integrated transport equation for the positrons is thus reduced to:

$$\frac{\partial \phi_z(\mathbf{r})}{\partial z} = -\mu_z(\mathbf{r})\phi_z(\mathbf{r}) \tag{14}$$

where $\mu_z(\mathbf{r})$ is an attenuation coefficient relative to the axial flux given by:

$$\mu_z(\mathbf{r}) = \frac{\phi(\mathbf{r})}{\phi_z(\mathbf{r})}\left(\frac{\rho_e(\mathbf{r})}{\phi(\mathbf{r})}\int \sigma_{\mathrm{an}}(\mathbf{r},v)\,v f(\mathbf{r},\mathbf{v})\,d\mathbf{v}\right) \tag{15}$$

with $\phi(\mathbf{r}) = \int v f(\mathbf{r},\mathbf{v})\,d\mathbf{v}$ being the total velocity-integrated flux.

References

[1] A. Polity, F. Börner, S. Huth, S. Eichler, R. Krause-Rehberg, Defects in electron-irradiated Si studied by positron-lifetime spectroscopy, Phys. Rev. B 58 (16) (1998) 10363–10377, http://dx.doi.org/10.1103/PhysRevB.58.10363.

[2] S.E. Derenzo, Mathematical removal of positron range blurring in high resolution tomography, IEEE Trans. Nuc. Sci. 33 (1986) 565–569, http://dx.doi.org/10.1109/TNS.1986.4337166.

[3] C.S. Levin, E.J. Hoffman, Calculation of positron range and its effect on the fundamental limit of positron emission tomography system spatial resolution, Phys. Med. Biol. 44 (3) (1999) 781–799, http://dx.doi.org/10.1088/0031-9155/44/3/019.

[4] J.E. Martin, Physics for Radiation Protection, 2nd Edition., John Wiley & Sons, New York, 2006, http://dx.doi.org/10.1002/9783527618798.

[5] S.R. Thontadarya, N. Umakantha, Comparison of mass absorption coefficients of positive and negative beta particles in aluminum and tin, Phys. Rev. B 4 (5) (1971) 1632–1634, http://dx.doi.org/10.1103/PhysRevB.4.1632.

[6] J.R. Patrick, A.S. Rupaal, Transmission of low energy positrons and electrons through thin metallic foils, Phys. Lett. 35A (4) (1971) 235–236, http://dx.doi.org/10.1016/0375-9601(71)90357-4.

[7] C.C. Watson, L. Eriksson, A. Kolb, Physics and applications of positron beams in an integrated PET/MR, Phys. Med. Biol. 58 (3) (2013) L1–L12, http://dx.doi.org/10.1088/0031-9155/58/3/L1.

[8] R.D. Evans, The Atomic Nucleus, McGraw-Hill, New York, 1955.

[9] G.F. Knoll, Radiation Detection and Measurement, 2nd ed., John Wiley & Sons, New York, 1989.

[10] F. Salvat, J.M. Fernández-Varea, J. Sempau, PENELOPE-2011: A Code System for Monte Carlo Simulation of Electron and Photon Transport, OECD Nuclear Energy Agency, Issy-les-Moulineaux, France, 2011.

[11] E.A. McCutchan, Nuclear data sheets for $A = 68$, Nucl. Data Sheets 113 (6-7) (2012) 1735–1870, http://dx.doi.org/10.1016/j.nds.2012.06.002.

[12] T. Tabata, R. Ito, S. Okabe, An empirical equation for the backscattering coefficient of electrons, Nucl. Instr. Meth. 94 (3) (1971) 509–513, http://dx.doi.org/10.1016/0029-554X(71)90013-9.

[13] H. Herzog, H. Iida, C. Weirich, L. Tellmann, J. Kaffanke, S. Spellerberg, L. Caldeira, E. Rota-Kops, N.J. Shah, Influence from high and ultra-high magnetic field on positron range measured with a 9.4T MR-BrainPET, IEEE Nucl. Sci. Symp. Conf. Rec. (2010) 3410–3413, http://dx.doi.org/10.1109/NSSMIC.2010.5874439.

[14] A. Kolb, A.W. Sauter, L. Eriksson, A. Vandenbrouke, C.C. Liu, C. Levin, B.J. Pichler, M. Rafecas, Shine-through in PET/MR imaging: effects of the magnetic field on positron range and subsequent image artifacts, J. Nucl. Med. 56 (6) (2015) 951–954, http://dx.doi.org/10.2967/jnumed.114.147637.

[15] R.E. Robson, M.J. Brunger, S.J. Buckman, G. Garcia, Z.L. Petrović, R.D. White, Positron kinetics in an idealized PET environment, Sci. Rep. 6 (2015) 12674, http://dx.doi.org/10.1038/srep12674.

[16] N. Corngold, Classical transport of charged particles in a magnetic field, J. Math. Phys. 44 (2003) 4057–4077, http://dx.doi.org/10.1063/1.1591994.

[17] A. Banković, S. Dujko, R.D. White, J.P. Marler, S.J. Buckman, S. Marjanović, G. Malović, G. García, Z.L. Petrović, Positron transport in water vapour, New J. Phys. 14 (3) (2012) 035003, http://dx.doi.org/10.1088/1367-2630/14/3/035003.